

Realizing four-electron conversion chemistry for all-solid-state Li||2 batteries at room temperature

Cheng, Zhu; Liu, Hang; Zhang, Menghang; Pan, Hui; Sheng, Chuanchao; Li, Wei; Wagemaker, Marnix; He, Ping; Zhou, Haoshen

DOI

[10.1038/s41467-025-56932-5](https://doi.org/10.1038/s41467-025-56932-5)

Publication date

2025

Document Version

Final published version

Published in

Nature Communications

Citation (APA)

Cheng, Z., Liu, H., Zhang, M., Pan, H., Sheng, C., Li, W., Wagemaker, M., He, P., & Zhou, H. (2025). Realizing four-electron conversion chemistry for all-solid-state Li||2 batteries at room temperature. *Nature Communications*, 16(1), Article 1723. <https://doi.org/10.1038/s41467-025-56932-5>

Important note

To cite this publication, please use the final published version (if applicable). Please check the document version above.

Copyright

Other than for strictly personal use, it is not permitted to download, forward or distribute the text or part of it, without the consent of the author(s) and/or copyright holder(s), unless the work is under an open content license such as Creative Commons.

Takedown policy

Please contact us and provide details if you believe this document breaches copyrights. We will remove access to the work immediately and investigate your claim.

Realizing four-electron conversion chemistry for all-solid-state Li||I₂ batteries at room temperature

Received: 25 May 2024

Accepted: 5 February 2025

Published online: 18 February 2025

 Check for updatesZhu Cheng^{1,2,3}, Hang Liu^{1,3}, Menghang Zhang¹, Hui Pan¹, Chuanchao Sheng¹, Wei Li¹, Marnix Wagemaker², Ping He¹✉ & Haoshen Zhou¹✉

Rechargeable Li||I₂ batteries based on liquid organic electrolytes suffer from pronounced polyiodides shuttling and safety concerns, which can be potentially tackled by the use of solid-state electrolytes. However, current all-solid-state Li||I₂ batteries only demonstrate limited capacity based on a two-electron I⁻/I₂ polyiodides chemistry at elevated temperatures, preventing them from rivaling state-of-the-art lithium-ion batteries. Herein, we report a fast, stable and high-capacity four-electron solid-conversion I⁻/I₂/I⁺ chemistry in all-solid-state Li||I₂ batteries at room temperature. Through the strategic use of a highly conductive, chlorine-rich solid electrolyte Li_{4.2}InCl_{7.2} as the catholyte, we effectively activate the I₂/I⁺ redox couple. This activation is achieved through a robust I-Cl interhalogen interaction between I₂ and the catholyte, facilitated by an interface-mediated heterogeneous oxidation mechanism. Moreover, apart from serving as Li-ion conduction pathway, the Li_{4.2}InCl_{7.2} catholyte is demonstrated to show a reversible redox behavior and contribute to the electrode capacity without compromising its conductivity. Based on the I⁻/I₂/I⁺ four-electron chemistry, the as-designed all-solid-state Li||I₂ batteries deliver a high specific capacity of 449 mAh g⁻¹ at 44 mA g⁻¹ based on I₂ mass and an impressive cycling stability over 600 cycles with a capacity retention of 91% at 440 mA g⁻¹ and at 25 °C.

Rechargeable lithium-ion batteries, based on intercalation electrodes, have experienced significant advancements over the past few decades and continue to play a vital role in portable devices and electric vehicle markets today^{1,2}. However, intercalation electrodes are approaching their maximum capacity limitations since their structures can only accommodate a maximum of one lithium ion per formula unit for insertion and release. Even the extensively studied Li-rich electrodes can only incorporate less than two lithium ions per formula unit^{3,4}, limiting the specific capacities achievable. Furthermore, intercalation electrodes typically utilize transition metal elements like cobalt and

nickel, which are not only expensive but also environmentally detrimental⁵. Hence, it is crucial to discover and design cost-effective electrode materials capable of storing a greater number of lithium ions, enabling multi-electron reactions. This advancement is essential for achieving higher specific capacity and energy density in future energy storage systems.

As an emerging conversion electrode material, iodine (I₂) shows several fascinating advantages including high abundance, environmentally benign, and a satisfactory specific capacity of 211 mAh g⁻¹ derived from two-electron I⁻/I₂ redox reaction^{6,7}. Specifically, typical

¹Center of Energy Storage Materials & Technology, College of Engineering and Applied Sciences, Jiangsu Key Laboratory of Artificial Functional Materials, National Laboratory of Solid State Microstructures and Collaborative Innovation Center of Advanced Microstructures, Nanjing University, Nanjing, PR China.

²Section Storage of Electrochemical Energy, Radiation Science and Technology, Faculty of Applied Sciences, Delft University of Technology, Delft, The Netherlands. ³These authors contributed equally: Zhu Cheng, Hang Liu. ✉e-mail: pinghe@nju.edu.cn; hszhou@nju.edu.cn

liquid Li||I_2 batteries exhibit good rate capabilities attributed to the high solubility and rapid diffusion of polyiodides in organic liquid electrolytes. However, this advantage comes with a critical drawback in the form of polyiodide shuttling, which continuously consumes the Li inventory at the negative electrode, ultimately leading to the failure of the battery^{8,9} (Fig. 1). Replacing liquid electrolytes with solid-state electrolytes could perfectly avoid the polyiodide shuttle effect because the solid-state electrolytes only allow lithium ions to pass through. Simultaneously, the potential safety problem associated with liquid electrolytes can be well resolved by the use of inflammable and thermal stable solid-state electrolytes^{10,11}. By employing a hybrid solid electrolyte, recently our group has realized a “confined dissolution” polyiodides chemistry that enables long-life rechargeable all-solid-state (ASS) Li||I_2 batteries¹². Unfortunately, this battery can only show a satisfactory capacity of 200 mAh g^{-1} at elevated temperature, severely restricting its potential application scenarios. To compete with state-of-the-art lithium-ion batteries, ASS Li||I_2 batteries need to demonstrate the ability to operate at room temperature (RT), and more importantly, achieve higher capacity and energy density.

In conventional Li||I_2 batteries, the redox of I_2 electrode is realized via a two-electron I/I_2 process. In fact, iodine possesses multiple valence states (such as I^- , I_2 , I^+ , I^{3+} , and I^{5+}) and thus is capable of exhibiting multi-electron redox behavior^{13,14}. Recently Zhi's group¹⁵ and Liang's group¹⁶ reported the activation of I_2/I^+ redox couple in aqueous Zn||I_2 batteries. This is achieved by the utilization of high Cl^- concentration electrolytes, which offer a rich coordination environment for the formation of I-Cl interhalogen bonds. Based on the pioneering work in liquid system, we can boldly speculate that designing ASS Li||I_2 batteries with a similar four-electron chemistry could potentially lead to the simultaneous achievement of high-energy density and enhanced safety features.

Unlike in aqueous Zn||I_2 batteries, where the polyiodide species and Cl^- can permeate the entire I_2 electrode to form robust I-Cl interhalogen bonds easily, in ASS Li||I_2 batteries, both I_2 and the solid electrolyte are fixed at their local environments due to the immobile nature of solids. Consequently, in order to fully activate the I_2/I^+ redox in the solid system, it is necessary to establish sufficient interhalogen coordination environment near every I_2 particle. In addition, the strong oxidation property of I^+ also requires the solid electrolyte to possess high oxidation tolerance. Following this guideline, in this work we develop a four-electron ASS Li||I_2 battery by designing a $\text{I}_2/\text{Li}_{4.2}\text{InCl}_{7.2}$ (LIC7.2) nanocomposite electrode. Compared with normal Li_3InCl_6 (LIC6), LIC7.2 could offer a more abundant Cl coordination environment while retaining high-voltage stability and sufficient ionic

conductivity. Consequently, we anticipate a more robust I_2/I^+ redox behavior in the $\text{I}_2/\text{LIC7.2}$ electrode compared to the $\text{I}_2/\text{LIC6}$ electrode. On top of this, a reversible $\text{I}/\text{I}_2/\text{I}^+$ four-electron solid-phase conversion chemistry is successfully achieved, as unveiled by a series of Raman, X-ray photonic spectroscopy (XPS) measurements and density functional theory (DFT) calculations. This leads to a high coulombic efficiency close to 100% and a doubled specific capacity for the ASS Li||I_2 batteries (Fig. 1). Moreover, dissimilar to conventional ASS batteries where the catholyte merely acts as a fast ion transport channel, here LIC7.2 is demonstrated to offer a reversible capacity without compromising its convenient ion transport and stability over a voltage range of 2–4 V versus Li^+/Li . As a result, the designed ASS Li||I_2 batteries show long cycle life at a practical high areal capacity (1.42 mAh cm^{-2}) and at RT (specified as 25°C unless otherwise noted in the following section). The superior performance is also demonstrated at elevated temperature (60°C) and high areal capacity (6.75 mAh cm^{-2}) scenario. Furthermore, the as-fabricated ASS Li||I_2 pouch cell shows reliable safety characteristic in cut tests. This work enriches the fundamental understanding of solid-phase reaction chemistry of I_2 electrode and will inspire more researches to explore novel ASS battery systems with high-energy densities.

Results and discussion

Activation of I_2/I^+ redox in ASS Li||I_2 batteries

The key to whether iodine molecules can undergo a four-electron reaction in an ASS system lies in the oxidation of zero-valent iodine to positively charged iodine. The local environment in the vicinity of the I_2 particles, as provided by the catholyte, plays a crucial role in this process. Building upon previous research on aqueous chlorine-concentrated Zn||I_2 batteries, here we utilize halide solid electrolytes as the catholyte in an endeavor to trigger the I_2/I^+ redox reaction through interhalogen bonds. Chloride LIC6 and bromide Li_3YBr_6 (LYB) are first considered as the catholyte candidates. Prior to mixing them with I_2 particles, charge tests were conducted on electrodes without iodine, only with electrolyte (LIC6 or LYB) and conductive agent carbon, to observe the oxidation behavior of the electrolytes themselves. The LIC6 and LYB exhibit capacities of 29.5 mAh g^{-1} and 14.4 mAh g^{-1} , respectively (Fig. 2a), attributed to the oxidation of the halide elements¹⁷, since In and Y element are already at their highest oxidation state of +3. Then nanocomposite I_2 electrode was prepared by mixing the LIC6 or LYB with I_2 and carbon via high-energy ball milling (denoted as $\text{I}_2/\text{LIC6}$ and I_2/LYB , respectively). As shown in Fig. 2b, the I_2/LYB electrode exhibits a negligible charging capacity,

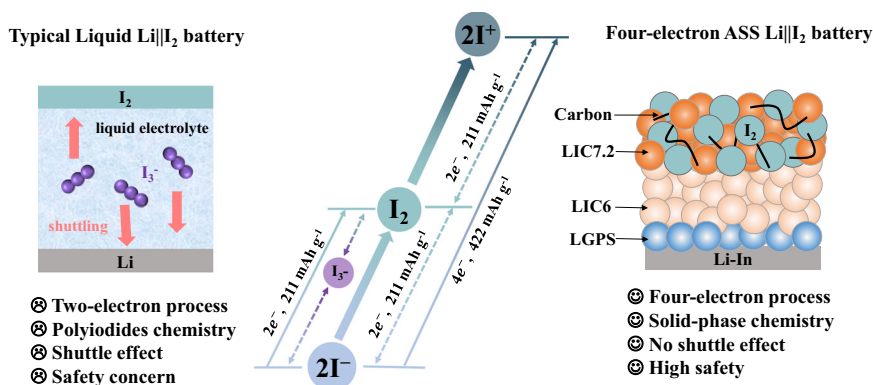


Fig. 1 | Schematic representations of liquid Li||I_2 batteries and LIC7.2-based ASS Li||I_2 batteries. Typical liquid Li||I_2 batteries show a theoretical capacity of 211 mAh g^{-1} based on two-electron I/I_2 polyiodides chemistry. The use of liquid electrolytes which dissolve polyiodides leads to severe shuttle effect and thus a low coulombic efficiency, as well as the potential safety concern. In the proposed ASS Li||I_2 batteries, a fast and reversible four-electron solid-phase conversion chemistry is achieved by the design of $\text{I}_2/\text{LIC7.2}$ composite electrode with a stable chlorine-rich environment, which

is capable of activating the I_2/I^+ redox couple. A doubled theoretical capacity of 422 mAh g^{-1} and high specific energy of $\sim 1302 \text{ Wh kg}^{-1}$ based on the active I_2 mass (434 Wh kg^{-1} based on the total mass of I_2 and LIC7.2) are demonstrated for the ASS Li||I_2 batteries. The use of LIC7.2 electrolytes perfectly eliminates the polyiodides shuttle problem and improves the safety. The crystalline LIC6 is used as the solid electrolyte layer due to its high ionic conductivity, and a layer of $\text{Li}_{10}\text{GeP}_2\text{S}_{12}$ (LGPS) is adopted between LIC6 and Li-In electrode to prevent the reduction of LIC6.

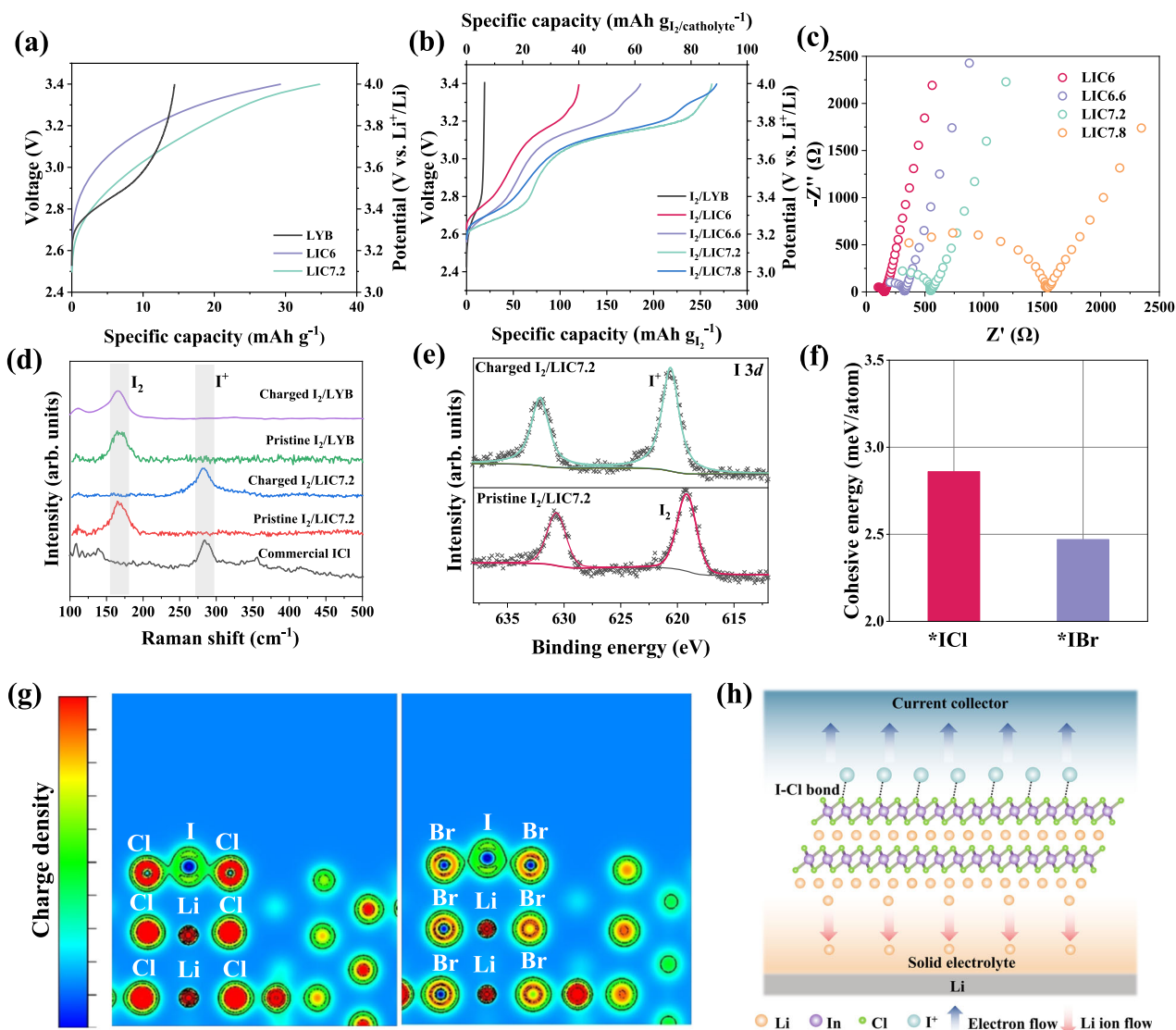


Fig. 2 | Electrochemical behavior of I_2 electrode in ASS batteries based on different electrolytes. **a** Direct charging voltage profiles of LYB, LIC6, and LIC7.2 as electrode materials. The specific capacity is calculated based on the mass of LYB, LIC6, or LIC7.2. **b** Direct charging voltage profiles of the I_2 /LYB, I_2 /LIC6, I_2 /LIC6.6, I_2 /LIC7.2, and I_2 /LIC7.8 electrode. The specific capacities based on the I_2 mass and the total mass of I_2 and catholyte are displayed in bottom and top x-axis, respectively. **c** Nyquist plots of the prepared LIC6, LIC6.6, LIC7.2, and LIC7.8. **d** Raman

spectra of the commercial ICl compound, pristine/charged I_2 /LYB and I_2 /LIC7.2 electrodes. **e** $13d$ XPS spectra of the pristine and charged I_2 /LIC7.2 electrode. **f** Two-dimensional charge densities distribution of *IBr in I_2 /LYB and *ICl in I_2 /LIC7.2. **g** Cohesive energies of the *IBr in I_2 /LYB and *ICl in I_2 /LIC7.2 obtained from DFT calculations. **h** Schematic of the interface-mediated heterogeneous oxidation mechanism facilitated by the substantial nanointerface between I_2 and LIC7.2 during the charging process of I_2 /LIC7.2 electrode.

indicating that I_2 cannot undergo effective oxidation in the bromide-based electrolyte. On the contrary, a higher capacity of 120 mAh g^{-1} is attained for the I_2 /LIC6 electrode. The charging plateau at 3.3 V versus Li^+/Li with a capacity around 60 mAh g^{-1} is attributed to the conversion of reduced polyiodides species to I_2 . During the ball-milling process, I_2 , with its strong electron absorption capability, induces electron transfer from KB to I_2 and therefore leads to the formation of reduced polyiodides species such as I_5^- and I_3^- ^{12,18}. As the conversion from I_5^- to I_2 has a theoretical capacity of 42.2 mAh g^{-1} , there is most likely a small amount of other further reduced polyiodides species (I_3^-) existing in the pristine electrode. The second charging plateau at 3.75 V versus Li^+/Li likely results from the oxidation of I_2 . The oxidation of Cl^- , which typically occurs at a higher potential, appears to be suppressed here, possibly due to a strong I-Cl interaction. However, this capacity is significantly lower than the theoretical capacity (211 mAh g^{-1}) of the two-electron I_2/I^+ conversion. This indicates that while the chloride solid electrolyte LIC6 has the

potential to activate the oxidation of I_2 , it cannot induce the complete I_2/I^+ redox couple. This limitation is likely due to the insufficient chlorine concentration surrounding the I_2 particles.

To enhance the localized chlorine concentration around the I_2 particles, it is necessary to increase the chlorine content in the LIC6 catholyte. At the same time, a high ionic conductivity for the catholyte is also required to provide efficient Li-ion transport within the I_2 electrode. Therefore, a series of Cl-concentrated Li-In-Cl solid electrolytes, namely $Li_{3.6}InCl_{6.6}$ (LIC6.6), $Li_{4.2}InCl_{7.2}$ (LIC7.2), and $Li_{4.8}InCl_{7.8}$ (LIC7.8) were synthesized by one-step ball-milling process. Supplementary Fig. 1 shows the X-ray diffraction (XRD) patterns of these Li-In-Cl series. All of them can be indexed with a C2/m space group, while some minor peaks corresponding to LiCl are shown in the XRD pattern of LIC7.8. This implies that the LIC7.8 stoichiometry is out of the Li-In-Cl solid solution range. Electrochemical impedance spectroscopy (EIS) measurements were conducted to obtain the ionic conductivities of the above-prepared Li-In-Cl solid electrolyte. With

increasing Cl content, the ionic conductivity drops from 0.63 mS/cm for LIC6 to 0.06 mS/cm for LIC7.8 (Fig. 2c). To evaluate their capabilities to activate the I_2/I^+ redox couple, I_2 composite electrodes based on these catholytes were subjected to direct charging tests. As displayed in Fig. 2b, the charge capacities for $I_2/LIC6$, $I_2/LIC6.6$, $I_2/LIC7.2$, and $I_2/LIC7.8$ electrodes are 120, 186, 261, and 267 mAh g⁻¹, respectively. It is clear that enough high Cl content in the Li–In–Cl catholyte (Cl ≥ 7.2 in Li–In–Cl) is required to fully activate the I_2/I^+ redox reaction. As a result, to achieve both efficient ionic transport and full utilization of I_2/I^+ redox couple, the LIC7.2 with high Cl content and a satisfactory ionic conductivity of 0.18 mS cm⁻¹ is selected as the optimized catholyte in this system. The Rietveld refinement results (Supplementary Fig. 2 and Tables S1 and S2) and ⁶Li solid-state magic angle spinning nuclear magnetic resonance measurements (Supplementary Fig. 3) further demonstrate that the stoichiometry LIC7.2 is a pure phase without any crystalline or amorphous unreacted precursors. Elemental mapping (Supplementary Fig. 4 and Table S3) also corroborated the expected stoichiometry of the prepared LIC7.2. It should be noted that the LIC7.2 alone can only exhibit a charge capacity of 35 mAh g⁻¹ (Fig. 2a), whereas the $I_2/LIC7.2$ electrode exhibits a much higher specific capacity of 265 mAh g⁻¹ (Fig. 2b). The plateau at 3.75 V versus Li⁺/Li, corresponding to the oxidation of I_2 molecules, accounts for a capacity of 190 mAh g⁻¹, which is very close to the theoretical capacity of the I_2/I^+ redox couple.

Ex situ Raman measurements were performed to get insight into the evolution of I_2 species in the composite I_2 electrode. As a comparison, the Raman spectra of both I_2/LYB and $I_2/LIC7.2$ electrode at pristine and charged states are displayed in Fig. 2d. Clear Raman shift at -162 cm⁻¹ of I_5^- , as the major reduced I_2 species, is observed for pristine I_2/LYB and $I_2/LIC7.2$ electrodes. After direct charging, no difference is found in the Raman spectrum of the I_2/LYB electrode, proving that I_2 cannot be oxidized with the LYB catholyte. In contrast, the I_5^- signal disappears and a new Raman shift located at -280 cm⁻¹ emerges for the charged $I_2/LIC7.2$ electrode. This Raman signal is also evident for commercial ICl compound, indicating the existence of the interhalogen bonds in the charged $I_2/LIC7.2$ electrode. This is consistent with the solid-state UV-Vis spectroscopy results (Supplementary Fig. 5), which show a strong absorption peak at around 350 nm—a characteristic peak of ICl interhalogen formation¹⁶ for the charged $I_2/LIC7.2$. Further confirmation of this I_2/I^+ conversion comes from the XPS results, showing that the I_2 (619.5 eV) in the pristine $I_2/LIC7.2$ electrode is oxidized to I^+ (620.5 eV) after being charged to 4 V versus Li⁺/Li (Fig. 2e). Based on above results, it can be inferred that the interhalogen bond between Cl⁻ and I^+ is more robust than that between Br⁻ and I^+ . This explains why the I_2/I^+ conversion is not activated for the I_2/LYB electrode.

To better understand the important role of chlorine in activating I_2/I^+ redox couple, DFT calculations were conducted on the $I_2/LIC7.2$ and I_2/LYB substrates (Supplementary Fig. 6). *ICl (*IBr) represents the interhalogen interaction between LIC7.2 (LYB) and I^+ species. A higher cohesive energy value is obtained for $I_2/LIC7.2$ than I_2/LYB , proving that the interhalogen interaction between I_2 and LIC7.2 is more thermodynamically favorable than that between I_2 and LYB (Fig. 2f). The related electron localization function was carried out to analyze the distribution of lone pair electron of the interhalogen phases. As shown in Fig. 2g, much more charges are found to distribute between I–Cl bonds in $I_2/LIC7.2$ than I–Br bonds in I_2/LYB , reflecting a more stable and robust electrical coupling between LIC7.2 and I^+ . This is also consistent with the Bader charge calculations showing that more charges are transferred between I and Cl (Supplementary Fig. 6a). Besides, the calculated bond length is shorter for I–Cl in $I_2/LIC7.2$ than I–Br in I_2/LYB (Supplementary Fig. 6b), indicating a more robust binding and stronger interaction between LIC7.2 and I^+ species. This suggests a lower energy barrier for the I_2/I^+ conversion in a LIC7.2-based system.

During the charging process, oxidation and Li-ion extraction typically occur within the same phase for intercalation electrodes, such

as LiCoO₂. These electrodes generally exhibit sufficient Li-ion diffusivity, allowing the delithiation process to occur easily in bulk form. However, for conversion electrodes with poor Li-ion mobility, the achievable capacity is highly dependent on their particle size. Smaller particle sizes lead to substantial interfaces between particles for conversion reaction to take place thus maximizing capacity release. This interface-mediated heterogeneous oxidation mechanism has been reported and widely acknowledged for conversion-type metal oxide electrode materials^{19–21}. For example, for the Co/Li₂O composite electrode, when the material's size is at the micron scale, its capacity is quite limited, and only at the nanoscale can it achieve a significantly large specific capacity during charging (over 600 mAh/g)²⁰. During charging, nanoscale Co undergoes an interface-mediated heterogeneous oxidation induced by the interface with Li₂O. As Li₂O releases lithium ions, oxygen ions bind to the Co atoms on the surface of the metallic Co, with these Co atoms simultaneously losing electrons, forming Co₃O₄. Both metallic Co and the charging product Co₃O₄ have poor ionic conductivity for oxygen ions. However, Co/Li₂O can still achieve a high charging capacity and a considerable amount of Co₃O₄ conversion. This is the result of interfacial-induced heterogeneous oxidation reactions at the nanoscale. A similar reaction occurs in the $I_2/LIC7.2$ electrode as shown in Fig. 2h and Supplementary Fig. 7. Nanoscale iodine and lithium halide electrolyte also form a pair of charging reactants. During the charging process, the lithium halide electrolyte ($I_2/LIC7.2$) releases lithium ions, and the halide ions bind to the iodine on the surface of the iodine particles. At the same time, the iodine molecules lose electrons and bond with Cl ions to form interhalogen. Of course, the halide electrolyte can only conduct lithium ions, but at the nanoscale, $I_2/LIC7.2$ electrode can still achieve a high conversion rate and large capacity by interface-mediated heterogeneous oxidation reaction. It should be pointed out that the difference between Co/Li₂O and $I_2/LIC7.2$ systems is that, Co atoms ionically bond with O atoms after charging, while the activated I ions covalently bond with Cl ions. This is because (1) I and Cl are both nonmetals and form a bond by sharing electron pairs, (2) the difference in electronegativity between I and Cl is not large enough to create an ionic bond. To achieve a high conversion efficiency as possible for the I_2/I^+ redox reaction, super intense ball-milling process (500 rpm for 12 h in WC jars) is employed to create substantial nanointerface in the composite $I_2/LIC7.2$ electrode. As a result, a large amount of I_2 and LIC7.2 domains with a size of several nanometers are created during this ball-milling process, as seen in the transmission electron microscopy image in Supplementary Fig. 8a. This nanoscale homogenous mixing is further demonstrated by energy-dispersive X-ray mapping shown in Supplementary Fig. 8b. For comparison, a hand-ground $I_2/LIC7.2$ electrode with inadequate contact interfaces is also tested, resulting in a significantly lower capacity of just 23 mAh g⁻¹ (Supplementary Fig. 9). This further proves the interface-mediated reaction mechanism for I_2/I^+ conversion and emphasizes the critical role of electrode preparation methods in achieving high conversion capacity for the I_2/I^+ reaction.

Four-electron conversion reaction mechanism

The activation of the two-electron I_2/I^+ process has been successfully demonstrated for the $I_2/LIC7.2$ electrode. However, it is still questionable whether a reversible I_2/I^+ process and the whole four-electron reaction can be realized. To investigate this, we conducted discharge/charge experiments on the LIC7.2-based ASS Li||I₂ battery, focusing on the first cycle (a two-electron process) and the second cycle (a four-electron process). As I_2 is the middle valence state between I^- and I^+ , the $I_2/LIC7.2$ electrode can be charged first to I^+ or discharged first to I^- . The battery is first discharged to 2 V versus Li⁺/Li here and then recharged to 4 V versus Li⁺/Li (Supplementary Fig. 10a). Note that the capacities are based on active I_2 mass in the $I_2/LIC7.2$ electrode. During the first discharge, a capacity of 242 mAh g⁻¹ is attained, most likely

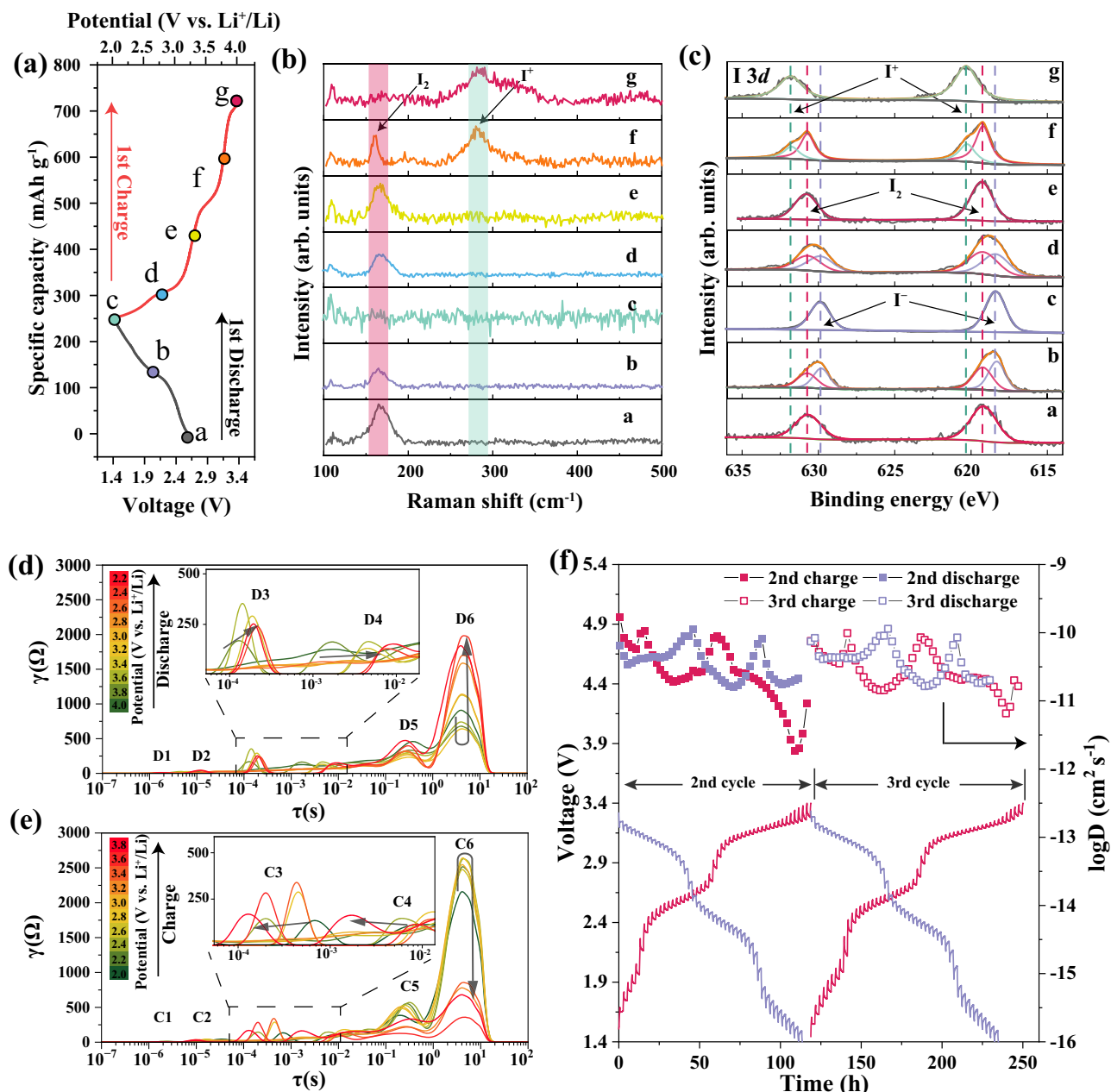


Fig. 3 | Characterizations of the reaction mechanism and kinetics for LIC7.2-based ASS Li||I₂ batteries. **a** First cycle discharge/charge curve of the I₂/LIC7.2 electrode. The specific capacity is calculated based on the mass of I₂. **b** Ex situ Raman spectra of the I₂/LIC7.2 electrode at stages a–g corresponding to the stages shown in (a). **c** Ex situ XPS spectra of the I₂/LIC7.2 electrode at stages a–g corresponding to the stages shown in (a). **d** DRT analysis of the discharge process for Li||I₂/LIC7.2 battery at the second cycle. **e** DRT analysis of the charging process for the

Li||I₂/LIC7.2 battery at the second cycle. **f** GITT curves and the corresponding calculated diffusion coefficients of the Li||I₂/LIC7.2 battery at the second and third cycles. Each constant current-rest step consisted of a 0.02 mA cm⁻² current pulse of 30 min and a 2 h relaxation. For these ex situ characterizations, the employed I₂/LIC7.2 electrode with 25% of active I₂ and an I₂ mass loading of 2 mg cm⁻² is electrochemically tested at 22 mA g⁻¹ with a voltage window of 2–4 V vs. Li at 25 °C.

corresponding to the transformation from I₂ to I⁻. During the subsequent recharge process, the battery displays three distinct plateaus (which will be discussed in the next section), with a noteworthy doubling of capacity observed at around 477 mA h g⁻¹. A similar discharge/charge behavior and a high capacity of around 420 mA h g⁻¹ is observed for the battery at the second cycle. When the battery is first charged to 4 V versus Li⁺/Li and then discharged to 2 V versus Li⁺/Li for the first cycle, it still shows a similar voltage profile and capacity value for the second cycle (Supplementary Fig. 10b), providing compelling evidence for the highly reversible nature of the I₂ redox reaction in this system.

As the crystallinity of iodine gets destroyed during high-energy ball-milling process (Supplementary Fig. 11), XRD was unable to distinguish various I₂ species at different states of charge (SOC). To unveil the detailed reaction mechanism of I₂/LIC7.2 electrode in the four-electron conversion ASS Li||I₂ battery, both ex situ Raman and XPS measurements were carried out on I₂/LIC7.2 electrode at different SOC to monitor the evolution of I₂ species. The SOC for Raman and XPS measurements are marked in the discharge-charge profile in Fig. 3a. At open circuit voltage, stage a in Fig. 3b, a strong Raman signal shows at ~160 cm⁻¹, which becomes weaker at a deeper discharge state of 2.6 V versus Li⁺/Li (stage b) and could be hardly observed after full discharge

to 2 V versus Li⁺/Li because of the insensitivity of I⁻ to Raman measurements (stage c). This indicates the transformation from I₂ to I⁻ (2e⁻) during the discharge process. In the following charge process, the Raman signal located at -160 cm⁻¹ appears again when the battery is charged to 2.8 V versus Li⁺/Li (stage d) and continues to grow after charging to 3.25 V versus Li⁺/Li (stage e), corresponding to the oxidation process from I⁻ to I₂. The I₂ signal intensity decreases when the electrode is further charged to 3.7 V versus Li⁺/Li (stage f). In addition, a strong stretch of I–Cl bond starts to emerge at -280 cm⁻¹, proving that the I₂ is successfully oxidized to I⁺. A full I₂/I⁺ conversion is achieved after the electrode is charged to 4 V versus Li⁺/Li (stage g), accompanied by the disappearance of I₂ Raman signal. It should be pointed out that this whole four-electron conversion process does not involve the dissolution-state polyiodides since the Raman shift at -116 cm⁻¹ corresponding to I₃⁻ is not observed during the measurements, which are commonly seen in previous liquid²² or polymer-based²² Li||I₂ batteries. This is the first time that a reversible solid-phase conversion was demonstrated in ASS Li||I₂ batteries, and therefore, no detrimental shuttle effect is expected.

The evolution of valence state change of I₂ species is precisely probed by XPS measurements at exactly the same SOCs with Raman measurements (Fig. 3c). From stage a to stage c which corresponds to the discharge process, the strong peak located at -619 eV (I₂) is found to decrease and then vanish, while the XPS signal peak at -618 eV (I⁻) grows with a deeper states of discharge (SOD). In the following charge process (stage d–g), XPS signal of I⁻ disappears at a charge state of 3.25 V versus Li⁺/Li (stage e) and I₂ signal becomes stronger, corresponding to the I⁻/I₂ conversion at 2–3.25 V versus Li⁺/Li. After charging to stage f, besides the XPS signal of I₂, another dominant peak can be observed at -620.5 eV, indicating that I₂ is oxidized to I⁺ under the inducing effect of LIC7.2. As expected, only I⁺ peak at -620.5 eV is detected at the charge cutoff voltage of 4 V versus Li⁺/Li (stage g).

To verify the fast and reversible kinetics in I₂/LIC7.2-based ASS Li||I₂ batteries with a four-electron chemistry, the battery resistance evolution was further studied by the in situ EIS measurements (Supplementary Fig. 12). The distribution of relaxation times (DRT) analysis was conducted at various SOD and SOC in order to provide a more intuitive representation of how the resistance of each component of the battery evolves throughout the cycling processes (Fig. 3d, e). Six dominant peaks can be identified in the time scale shown, which correspond to different kinetic processes with distinct time constants. During the whole discharge/charging process, the D1/C1 peak ranging between 10⁻⁶ s and 10⁻⁵ s representing the grain boundary resistance of the solid electrolyte²³ is almost submerged by the noise or inductance signal at super high frequencies. The D2/C2 peak located around 10⁻⁵ s corresponds to the contact resistance between electrode and current collectors. The peaks with the intermediate processes are attributed to the charge transfer behavior at the LIC6/Li₁₀GeP₂S₁₂ (LGPS) interface (D3/C3, LIC6, and LGPS are used as a dual-layer electrolyte here), Li–In negative electrode/LGPS interface (D4/C4) and I₂/LIC7.2 electrode/LIC6 interface (D5/C5). As the solid-state diffusion within the I₂/LIC7.2 electrode is the most sluggish process, it shows the largest time constant above 10⁰ s and is assigned to the D6/C6 peak. During the discharge process, the D6 peak shows a decrease during the first several measurements where the transformation from I⁺ to I₂ is anticipated. Afterward, an increase in intensity is observed for D6 along the following discharge process, indicating a slower diffusion within the I₂/LIC7.2 electrode. In the subsequent charge process, the intensity of C6 peak slightly increases at first and then decreases until the battery is fully charged. Similarly, reversible charge transfer processes at the interfaces are also observed. Time constants of the charge transfer processes at LIC6/LGPS and Li–In negative electrode/LGPS interfaces shift to a larger value during discharge (D3 and D4 peak) and then shift back to their original states during charge. Comparing the beginning of discharge and end of charge states, all the C1–C6 peaks show almost

the same intensities and shifts as D1–D6 peaks, implying that the solid-phase four-electron chemistry is highly reversible. This is further verified by the galvanostatic intermittent titration technique (GITT) measurement (Fig. 3f). The GITT experiment was carried out on the battery during the second and the third cycles, with each step consisting of a 30-min charge/discharge at a constant current of 0.02 mA cm⁻² and a 2 h rest process. Lithium diffusion coefficients (D_{Li⁺}) during these two cycles are calculated from the GITT measurements. At the initial states of both I⁻/I₂ and I₂/I⁺ solid-phase reactions, D_{Li⁺} values are relatively high and then gradually decrease afterward. During the whole two cycles, the D_{Li⁺} is in the range of 10⁻¹¹ and 10⁻¹⁰ cm² s⁻¹ except at the end of charge, indicating a fast kinetics of this I⁻/I₂/I⁺ solid-phase conversion chemistry. The evolution trend and value of D_{Li⁺} are nearly the same for the second and the third cycle, which again demonstrates the reversibility of this four-electron I⁻/I₂/I⁺ conversion mechanism.

Capacity contribution of LIC7.2 catholyte

As mentioned above, three discharge/charge plateaus are observed in the voltage profile of I₂/LIC7.2 electrode. Similarly, three pairs of redox peaks could also be well defined in its cyclic voltammetry (CV) curves within the operation voltage window of 2–4 V versus Li⁺/Li (Fig. 4a). The cathodic peak at -2.75 V versus Li⁺/Li (E_{c,2}) and anodic peak at -3.3 V (E_{a,2}) are rationally ascribed to the reversible reaction between I₂ and I⁻, while the pair of peaks of E_{c,3} (-3.6 V versus Li⁺/Li) and E_{a,3} (-3.75 V versus Li⁺/Li) is attributed to the I₂/I⁺ redox couple. According to previous DFT studies^{24,25}, the indium-based halide electrolyte would be reduced at voltages lower than 2.3 V versus Li⁺/Li, which falls within the cycling voltage range of the ASS Li||I₂ battery (2–4 V versus Li⁺/Li). Therefore, the third pair of redox peaks (E_{c,1} and E_{a,1}) centered at around 2.3 V versus Li⁺/Li is most likely attributed to the In³⁺/In²⁺ redox couple in LIC7.2 catholyte.

To clarify the redox activity of LIC7.2 catholyte in the I₂/LIC7.2 composite electrode, LIC7.2 mixed with KB was used as the positive electrode to perform CV tests. Within a voltage range of 2–4 V versus Li⁺/Li, a cathodic peak E_{c,1}' (located at -2 V versus Li⁺/Li) and two anodic peaks E_{a,1}' and E_{a,4}' (located at 2.75 V versus Li⁺/Li and 4 V versus Li⁺/Li, respectively) can be observed (Fig. 4b). When the CV scans are conducted at 2.4–4 V versus Li⁺/Li, as seen in Supplementary Fig. 13, no obvious cathodic peaks can be distinguished and E_{a,1}' anodic peak disappear as well. Therefore, both E_{c,1}' and E_{a,1}' come from the redox reaction of In³⁺/In²⁺, while E_{a,4}' is attributed to the oxidation of Cl⁻ according to previous work²⁶. Importantly, E_{c,1}'/E_{a,1}' redox pair of LIC7.2 electrode occurs at a similar potential to E_{c,1}/E_{a,1} redox pair of I₂/LIC7.2 electrode, proving that the E_{a,1} and E_{c,1} peaks in the I₂/LIC7.2 electrode indeed come from the LIC7.2 catholyte. It should be pointed out that the E_{a,4}' peak corresponding to the Cl⁻ oxidation in LIC7.2 disappears in the CV curves of I₂/LIC7.2 electrode, indicating that Cl⁻ redox behavior of LIC7.2 is different from that of I₂/LIC7.2 electrode. This could be explained by the robust I–Cl interhalogen interaction between activated I⁺ and Cl⁻, which suppresses the oxidation of Cl⁻ within this voltage range.

The capacity contribution of LIC7.2 redox activity to the I₂/LIC7.2 electrode capacity was quantified by galvanostatic cycling test of the LIC7.2 electrode following a charge-discharge sequence. As shown in Fig. 4c, during the first charge, the LIC7.2 delivers a capacity of 27 mAh g⁻¹ derived from the oxidation of Cl⁻. The subsequent discharge process reveals a capacity of 62 mAh g⁻¹ mainly attributed to the reduction of In³⁺. However, by the second cycle, the charging plateau associated with Cl⁻ almost disappears, implying that the Cl⁻ redox reaction of LIC7.2 is not reversible. Furthermore, the discharging capacity linked to the In³⁺/In²⁺ redox initially decreases but stabilizes by the tenth cycle. Notably, a stable capacity of 25 mAh g⁻¹ is observed for the LIC7.2 electrode after 10 cycles (Fig. 4d). Given that the mass ratio of LIC7.2 to I₂ is 2:1 in the I₂/LIC7.2 electrode, it is evident

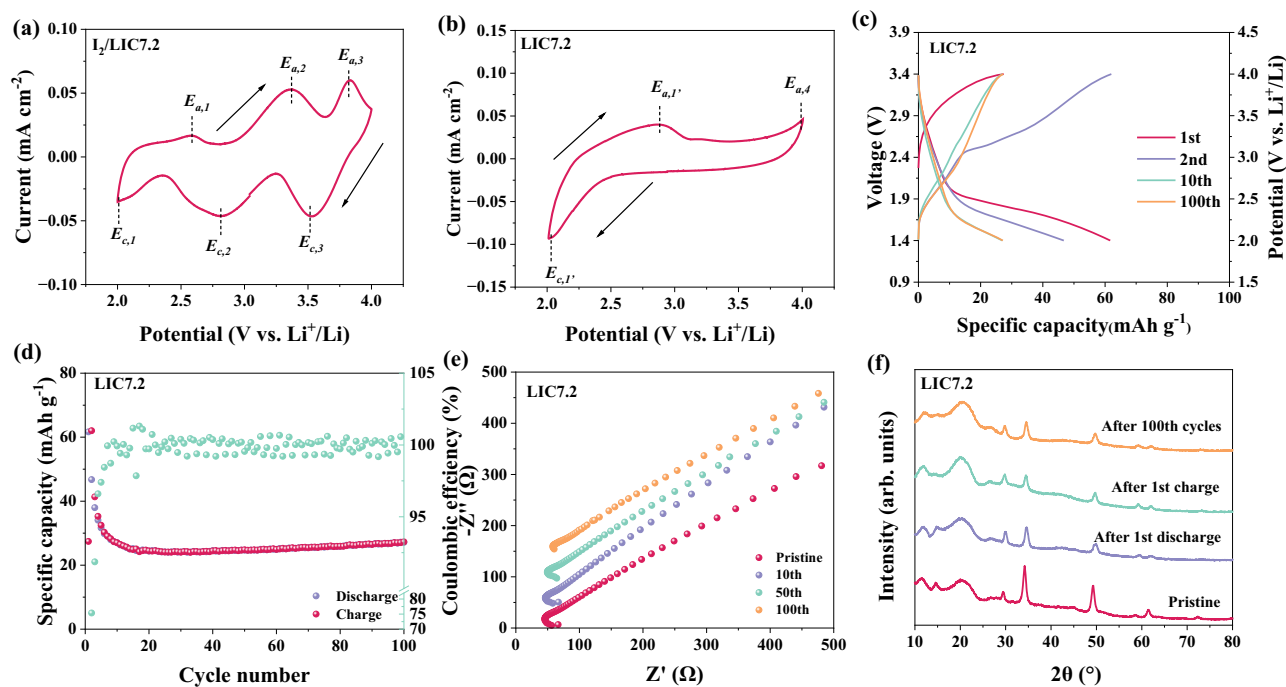


Fig. 4 | Redox activity of LIC7.2. **a** Cyclic voltammetry curves of the $I_2/LIC7.2$ electrode (The I_2 mass loading is 0.5 mg cm^{-2}) at a sweep rate of 0.1 mV s^{-1} . **b** CV curves of the LIC7.2 electrode (The LIC7.2 mass loading is 2 mg cm^{-2}) with a sweeping voltage range of 2–4 V versus Li⁺/Li at a sweeping rate of 0.1 mV s^{-1} . **c** Voltage profiles of the LIC7.2 electrode at the 1st, 2nd, 10th, and 100th cycle. The electrode was charged first and then discharged. The specific capacity is calculated

based on the mass of LIC7.2. **d** Cycling stability of the LIC7.2 electrode at a current of $40 \mu\text{A cm}^{-2}$. The specific capacity is calculated based on the mass of LIC7.2. **e** Nyquist plots of the LIC7.2 electrode-based battery at the pristine state and after 10, 50, and 100 cycles. **f** XRD patterns of the LIC7.2 electrode at pristine, discharged, recharged states and after 100 cycles.

that the redox reaction of LIC7.2 contributes to a specific capacity of 50 mAh g^{-1} after 10 cycles in the $I_2/LIC7.2$ electrode.

Based on the above analysis, it can be inferred that the redox behavior of LIC7.2 comprises two distinct components: the $\text{In}^{3+}/\text{In}^{2+}$ redox and the Cl^- redox. In the $I_2/LIC7.2$ composite, a consistent $\text{In}^{3+}/\text{In}^{2+}$ redox reaction is observed, while the Cl^- oxidation of LIC7.2 is notably suppressed due to the strong interaction between I^+ and Cl^- ions. This difference in behavior suggests that the activation of I_2/I^+ redox reaction alters the Cl^- redox activity of LIC7.2. The reduction or oxidation of solid electrolytes is generally believed to compromise their conductivity, leading to poor lithium-ion transfer within batteries. Contrarily, the sole LIC7.2 electrode maintains stable cycling performance over 100 cycles, with no significant changes in battery resistance observed after extensive cycling, as shown in Fig. 4e. These observations prove that the redox behavior of LIC7.2 does not adversely affect its ionic conductivity. Previous studies have indicated that solid electrolytes, such as $\text{Li}_6\text{PS}_5\text{Cl}$, initially undergo lithiation/delithiation processes, subsequently converting into thermodynamically stable but poorly conductive decomposition products^{27,28}. These products hinder ionic transport across the electrode/solid electrolyte interface. However, unlike sulfide-based electrolytes, the redox reaction in LIC7.2 does not lead to its direct decomposition, as evidenced by the XRD patterns of the LIC7.2 electrode at pristine, charged, discharged and 100-cycled states shown in Fig. 4f. Moreover, the LIC7.2 in the $I_2/LIC7.2$ composite electrode can also maintain good structural stability during cycling, as confirmed by XRD results (Supplementary Fig. 14). Note that a slight shift of the XRD peaks is observed for the charged and discharged samples, further proving a reversible lithiation/delithiation behavior of the LIC7.2. This good stability is further supported by the EIS results for the LIC7.2 electrode-based battery during its first cycle, presented in Supplementary Fig. 15. The overall resistances in different states of the battery (pristine, discharged, and charged) show comparable values, indicating that LIC7.2 maintains rapid lithium-ion kinetics throughout the redox process.

In typical ASS batteries, catholytes primarily serve as pathways for rapid ion transport. When the cutoff voltage exceeds the thermodynamic stability window of the electrolyte, severe decomposition can occur, contributing to irreversible capacity and obstructing efficient ion transport at the electrode/solid electrolyte interface. In contrast, LIC7.2 not only facilitates efficient ionic diffusion but also contributes reversible capacity through its redox activity while activating the I_2/I^+ redox couple. This triple functionality enhances the performance of the composite $I_2/LIC7.2$ electrode, underscoring the strategic advantage of employing LIC7.2 as the catholyte in ASS $\text{Li}||\text{I}_2$ batteries.

Electrochemical performance of the four-electron ASS $\text{Li}||\text{I}_2$ battery

To evaluate the electrochemical performance of the as-designed ASS $\text{Li}||\text{I}_2$ batteries based on $I_2/LIC7.2$ electrode, a series of galvanostatic cycling tests were conducted. Unless otherwise specified, all capacity values below are calculated based on the mass of I_2 . Supplementary Fig. 16 displays the voltage profiles and long-term cycling stability of the battery at an I_2 mass loading of 0.5 mg cm^{-2} at RT. The battery delivers a high capacity of 430 mAh g^{-1} at the second cycle, and still maintains a capacity of $\sim 400 \text{ mAh g}^{-1}$ after 200 stable cycles, with a capacity retention of 93%. Because LIC7.2 contributes to the cell capacity during cycling, the specific capacity based on the total mass of I_2 and LIC7.2 is also presented in the figures. It is worth noting that an average coulombic efficiency of 99.03% is achieved for the battery from 5th to 200th cycle, validating the advantages of ASS $\text{Li}||\text{I}_2$ batteries over liquid-based $\text{Li}||\text{I}_2$ batteries which usually show much lower coulombic efficiencies due to the severe polyiodides shuttle effect. This advantage is further demonstrated by the self-discharge performance. A very stable voltage of 3.2 V versus Li⁺/Li could be maintained for 120 h after the battery assembly, which indicates there is no self-discharge (Supplementary Fig. 17a). When the battery is charged to 4 V

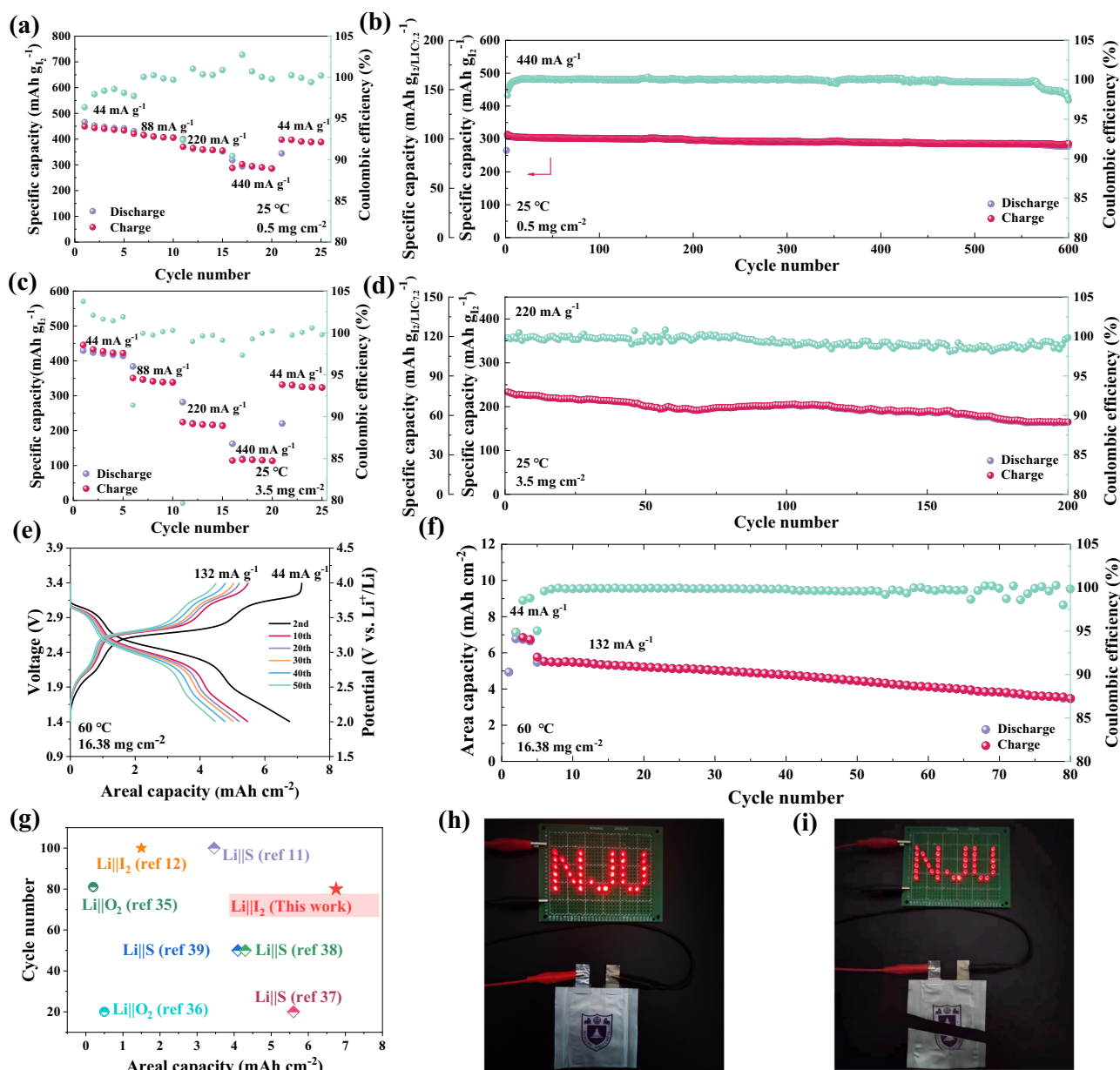


Fig. 5 | Electrochemical performance of the four-electron ASS Li||I₂ batteries.

a Rate performance of the battery with a mass loading of 0.5 mg cm^{-2} at RT. **b** Cycling stability with the corresponding coulombic efficiency of the battery at 440 mA g^{-1} and RT. The I₂ mass loading is 0.5 mg cm^{-2} . **c** Rate performance of the battery with a mass loading of 3.5 mg cm^{-2} at RT. **d** Cycling stability with the corresponding coulombic efficiency of the battery at 220 mA g^{-1} and RT. The I₂ mass loading is 3.5 mg cm^{-2} . Voltage profiles (**e**) and **f** cycling performance of the battery under high temperature ($60 \text{ }^\circ\text{C}$) and high mass loading (16.38 mg cm^{-2}) at a current of 132 mA g^{-1} . **g** Comparison of areal capacity and cycle life of four-electron ASS Li||I₂ batteries and literature-reported results on ASS batteries with conversion-type electrodes under high areal capacity condition. **h** Photograph of the ASS Li||I₂ pouch cell ($40 \times 40 \text{ mm}$ film-type battery in a $60 \times 60 \text{ mm}$ case) powering LED lights. **i** Illustration of the pouch cell showing high safety and well-running under the condition of being half-cut.

versus Li⁺/Li and then rests for 120 h, the voltage slowly drops to 3.75 V versus Li⁺/Li and then keeps stable (Supplementary Fig. 17b). The resulting coulombic efficiency of 93.03% surpasses that of reported I₂ electrodes in liquid Zn||I₂ batteries^{29–31}. The ASS Li||I₂ battery also displays exceptional rate performance (Fig. 5a), obtaining high discharge capacities of 449 mAh g^{-1} , 420 mAh g^{-1} , 370 mAh g^{-1} , and 302 mAh g^{-1} at 44 mA g^{-1} , 88 mA g^{-1} , 220 mA g^{-1} , and 440 mA g^{-1} respectively. When the rate is turned back to 88 mA g^{-1} , it still shows a discharge capacity of 400 mAh g^{-1} . To evaluate the fast and stable kinetics of I₂/I[•] chemistry, the battery is cycled at a high rate of 440 mA g^{-1} and delivers a high capacity of 278 mAh g^{-1} with a satisfying capacity retention of 91% for over 600 cycles (Fig. 5b). When the ASS Li||I₂ battery is cycled at a voltage range of $2.4\text{--}4 \text{ V}$ versus Li⁺/Li to exclude the capacity

contribution of LIC7.2 catholyte, it shows a lower capacity of 350 mAh g^{-1} for the second cycle and maintains a capacity of $\sim 200 \text{ mAh g}^{-1}$ after 400 cycles at 88 mA g^{-1} and RT (Supplementary Fig. 18). This means that partial capacity of the I₂/I[•] redox couple is also sacrificed at this narrower operation voltage window. Based on the above high performance, it is evident that cycling the battery at a voltage window of $2\text{--}4 \text{ V}$ versus Li⁺/Li is essential to utilize the full capacity of four-electron I₂/I[•] chemistry, and the redox behavior of LIC7.2 does not affect the stability of the battery and efficient ionic transport at all. To further demonstrate the good compatibility of the LIC7.2 catholyte with I₂ electrode, galvanostatic cycling was also conducted for I₂/LYB electrode-based ASS Li||I₂ battery (Supplementary Fig. 19). A lower capacity of $\sim 250 \text{ mAh g}^{-1}$ is observed, corresponding to

the two-electron Γ/I_2 process, which however decays to 170 mAh g^{-1} after only 8 cycles.

The electrochemical performance of the $I_2/LIC7.2$ based ASS $Li||I_2$ battery was further evaluated at harsh conditions such as high areal capacities and high temperatures. At an I_2 mass loading of 3.5 mg cm^{-2} , a high discharge capacity of $\sim 400 \text{ mAh g}^{-1}$ is obtained for the battery operating at 22 mA g^{-1} and at RT (Supplementary Fig. 20), corresponding to a high areal capacity of 1.42 mAh cm^{-2} . A good rate performance is also demonstrated at this high mass loading condition and at RT (Fig. 5c). Noting that the rate capability at 3.5 mg cm^{-2} is decreased compared to that at a lower mass loading of 0.5 mg cm^{-2} . This is attributed to the intrinsically low Li^+ diffusion coefficient of the conversion-type I_2 electrode. Moreover, at a high rate of 220 mA g^{-1} , it shows a satisfactory cycling stability and 83.6% capacity retention after 200 cycles (Fig. 5d). EIS measurements were conducted to monitor the evolution of battery resistance over this long-term cycling (Supplementary Fig. 21a). The electrolyte resistance (R_l) is 50Ω for the fresh battery, and keeps almost unchanged over 100 cycles and slightly grows to 73Ω after 200 cycles. The semicircle at middle-frequency range is difficult to distinguish for the fresh battery, indicating a very intimate $I_2/LIC7.2$ electrode/electrolyte interface contact. After 50 cycles, a semicircle could be observed in the EIS curve of the battery, corresponding to an interface resistance (R_2) of $\sim 10 \Omega$, which gently increases to $\sim 80 \Omega$ after 200 cycles. The corresponding DRT analysis is displayed in Supplementary Fig. 21b. No obvious change in the peak intensity can be found at the short time constant range (10^{-7} – 10^{-2} s). An increase of the intensities is observed for peaks at time constants above 10^{-2} s after 200 cycles, while the peak representing the ionic diffusion within $I_2/LIC7.2$ electrode with the longest time constant of ~ 1 s shows the biggest increase. The most plausible reason for the increased interface resistance would be the repeated volume change of the electrode during conversion reactions, which could lead to the worsening of ionic transport within the $I_2/LIC7.2$ electrode and gradual physical deterioration of the electrode/electrolyte interface^{32,33}. This also explains the relatively worse capacity retention of the battery with a higher mass loading (16.38 mg cm^{-2} , Fig. 5e, f) which experiences a more severe volume change than that with a low mass loading (0.5 mg cm^{-2} , Fig. 5b). At a harsh condition of a mass loading of 16.38 mg cm^{-2} and an elevated temperature of 60°C (Fig. 5e, f), an areal capacity of 6.75 mAh cm^{-2} (412 mAh g^{-1} based on I_2 and 137.4 mAh g^{-1} based on $I_2/LIC7.2$) is achieved at a current of 44 mA g^{-1} . Even at this high mass loading and high-temperature test condition, this battery shows a satisfying cycling stability over 80 cycles with a capacity retention of 72.2%. It should be noted that bare I_2 easily sublimates at temperature higher than 40°C . The effective trapping of I_2 inside the pores of KB avoids I_2 loss at 60°C in the $I_2/LIC7.2$ composite electrode (Supplementary Fig. 22), and leads to the above good high-temperature performance.

Compared to conventional intercalation-positive electrodes, conversion-type positive electrodes such as O_2 , S, and I_2 usually possess much higher specific capacities due to their ability to manifest multiple-electron chemistry. While S and O_2 have super high capacities (1672 mAh g^{-1} for S based on S mass and over 5000 mAh g^{-1} for O_2 based on the host material mass)³⁴, their application in ASS batteries still confronts severe challenges such as sluggish kinetics and huge overpotential. Thanks to the fast and stable four-electron $\Gamma/I_2/I^+$ conversion chemistry, the ASS $Li||I_2$ batteries exhibit much better kinetics and cycling stability than ASS $Li||S$ and $Li||O_2$ batteries, especially under a high areal capacity condition. In Fig. 5g our designed ASS $Li||I_2$ batteries and literature-reported ASS $Li||S/O_2$ batteries under high areal capacity condition are plotted in two dimensions of areal capacity and cycle number. Compared to two-electron conversion ASS $Li||I_2$ battery based on poorly conductive hybrid electrolyte¹², the four-electron ASS $Li||I_2$ battery based on LIC7.2 catholyte is able to operate at a six times

higher areal capacity (6.75 mAh cm^{-2}). Despite the high theoretical discharge capacity of O_2 electrode, current ASS $Li||O_2$ batteries^{35,36} are only able to operate at areal capacities less than 0.5 mAh cm^{-2} . Even compared with intensively studied ASS $Li||S$ batteries^{11,37–39} our ASS $Li||I_2$ battery still performs better at extreme areal capacity conditions. Last but not least, we further fabricated a pouch cell with dimensions of $40 \times 40 \text{ mm}$ and a capacity of 22 mAh to validate the potential application prospect of our ASS $Li||I_2$ battery (Supplementary Fig. 23). It is able to power LED lights (Fig. 5h) and still shows well-running after being half-cut (Fig. 5i). While the ASS $Li||I_2$ battery demonstrates high electrochemical performance and high safety, it is worth noting that the active I_2 mass in the $I_2/LIC7.2$ electrode only accounted for $\sim 25\%$. Further increasing the I_2 mass ratio to 40% leads to a very limited activation of the I_2/I^+ redox (Supplementary Fig. 24), which is attributed to the insufficient I–Cl coordination environment near the I_2 particles, as well as a worse ionic conductivity. To further improve the practical capacity of the I_2 positive electrode, it's crucial to develop advanced I_2 composite electrode structures with higher specific surface area and improved electronic/ionic conductivity. Simultaneously, investigating the I–Cl coordination mechanism in the solid-state system would aid in understanding the interplay between I_2 and the catholyte, which helps to optimize the usage of active I_2 and catholyte in the electrode and achieve higher energy density for ASS $Li||I_2$ batteries.

In summary, we have achieved an $\Gamma/I_2/I^+$ four-electron solid-phase conversion chemistry for ASS $Li||I_2$ battery through the employment of chlorine-rich catholyte LIC7.2. The as-synthesized LIC7.2 with high local Cl^- concentration provides sufficient coordination environment for the interhalogen interaction between I^+ species and Cl^- , effectively activating the complete I_2/I^+ conversion. Our proposed mechanism for this I_2/I^+ conversion involves an interface-mediated “heterogeneous oxidation” process, wherein the oxidation process occurs on the I_2 phase and the delithiation process occurs on the LIC7.2 catholyte phase. In contrast to typical catholytes, which primarily function as ionic pathways, the LIC7.2 catholyte showcases an additional capability –it actively contributes to the overall capacity through its redox activity, without compromising its efficient ionic conduction properties. Moreover, the utilization of highly conductive inorganic catholyte and electrolyte facilitates a direct solid-phase conversion between Γ , I_2 , and I^+ at RT. Consequently, ASS $Li||I_2$ batteries effectively circumvent the polyiodide shuttle effect commonly observed in liquid $Li||I_2$ batteries. This advancement results in a high discharge capacity of 449 mAh g^{-1} at 44 mA g^{-1} and long-term stability over 600 cycles at 440 mA g^{-1} at RT. Furthermore, the battery demonstrates stable cycling under practical high areal capacity (6.75 mAh cm^{-2}) and elevated temperature (60°C) conditions, while rigorous pouch cell cutting tests confirm its high safety profile. This study underscores the promising application potential of ASS $Li||I_2$ batteries in energy storage, particularly in scenarios requiring both high capacity and enhanced safety features, and would definitely garner increased attention towards the research of ASS batteries based on novel conversion positive electrodes.

Methods

Material synthesis

Ball milling was used to prepare the $I_2@KB$ powder. I_2 (Aladdin) and KB (EC-600JD) with a weight ratio of 1:1 were ball milled at 500 rpm for 12 h. The LIC6, LIC6.6, LIC7.2, LIC7.8, and LYB were synthesized by a one-step ball-milling process. The LIC6 and LIC7.2 were synthesized by ball-milling stoichiometry $LiCl$ (Sigma Aldrich, 99%) and $InCl_3$ (Alfa Aesar, 99.99%) at 600 rpm for 24 h. The LYB was synthesized by ball-milling stoichiometry $LiBr$ (Sigma Aldrich, 99.9%) and YBr_3 (Alfa Aesar, 99.9%) at 600 rpm for 24 h. The LGPS was purchased from Shenzhen MTI. The crystalline LIC6 was prepared through a water-mediated method reported elsewhere⁴⁰. To prepare the $I_2/LIC6$, $I_2/LIC6.6$, $I_2/$

LIC7.2, I₂/LIC7.8, and I₂/LYB composite electrodes, the I₂@KB powder with ~48 wt% I₂ and the catholytes was ball milled at 500 rpm for 12 h with a certain weight ratio (3:7 for 15 wt% I₂, 1:1 for 25 wt% I₂ and 4:1 for 40 wt% I₂). LIC6/LIC6.6/LIC7.2/LIC7.8/LYB-based electrodes were prepared by ball milling them with KB powder with a weight ratio of 1:2 at 400 rpm for 4 h. All the above ball-milling processes were performed using 45 mL WC jars containing 1 mm WC balls with a ball-to-powder ratio of 40:1. The hand-ground I₂/LIC7.2 electrode was prepared by milling the I₂@KB and LIC7.2 (weight ratio of 1:1) with a pestle and mortar for 30 min.

Material characterizations

Raman spectroscopy was conducted using a confocal Raman instrument (NTEGRA Spectra AFM Raman Confocal SNOM). The chemical composition and surface states were analyzed through X-ray photoelectron spectroscopy (XPS) on a PHI 5000 VersaProbe-II system. EIS was performed with a Solartron 1287/1290 system, applying a 5 mV perturbation voltage in a frequency range of 1 MHz to 0.1 Hz. Measurements included six data points per decade, with a 15-min resting period for the cell prior to each test. The obtained EIS data were analyzed using ZPlot software, and the DRT was evaluated with EISART software⁴¹. Thermal stability was assessed through thermogravimetric analysis using a TA SDTQ600 analyzer. The temperature was increased from RT (25 °C) to 600 °C at a rate of 10 °C/min under a nitrogen atmosphere. Structural characterization was carried out via XRD on a PHI 5000 VersaProbe system. The morphological features of the electrodes and electrolyte were observed with a Hitachi SU8010 scanning electron microscope, while detailed microstructural analysis was performed using a FEI TF20 transmission electron microscope at an operating voltage of 200 kV.

Cell assembly and electrochemical tests

Cell assembly was performed under inert conditions using an argon glove box, where the ASS batteries were constructed inside cylindrical housings made of PEEK material featuring a 10 mm inner diameter. First, 50 mg crystalline LIC6 with ionic conductivity over 1 mS cm⁻¹ was added to the mold and mechanically pressed at 300 MPa for 5 min. Then 50 mg LGPS powder as protective layer was spread on LIC6 and then pressed at 300 MPa for 5 min. I₂/LIC6, I₂/LIC7.2, I₂/LIC7.8, and I₂/LYB composite electrode was distributed evenly on the side of the LIC6 pellet. The thickness of the 50 mg solid electrolyte layer is 243 μm (Supplementary Fig. 25) with a porosity of 3.71% (Supplementary Fig. 26). The thickness of the I₂/LIC7.2 with a typical mass loading of 5.1 mg cm⁻² is 59 μm with a porosity of 7.44% (Supplementary Fig. 27). An In foil (with a diameter of 8 mm, thickness of 100 μm) was attached to the other side of LGPS pellet. A Li foil with a molar ratio of Li:In = 0.5:1 was pressed on the In foil and kept under 50 MPa for 4 h (Lithium foil was purchased from China Energy Lithium Co, ≥99.9%). The fabricated cells were rested for 6 h before testing. All cell assembly processes were carried out in an argon-filled glove box and cycled at a stacking pressure of 50 MPa. To manufacture solid-state pouch cells, LGPS, LIC6, and electrode films are prepared by mixing with PTFE (Daikin Industries) additives (mass ratio: ≈1%) and rolling into thin sheets (thickness: ≈0.05 mm). Pouch Li–In|LGPS–LIC6|I₂/LIC7.2 cells are made by pressing the LGPS, LIC6, and electrode films at 100 MPa and then pressing the Li–In foil onto one side of the LGPS film. The size of the LGPS and LIC6 films was 40×40 mm and the size of both the Li–In foil and the electrode film (I₂ loading: 62 mg) was 38×38 mm. Regarding the preparation of the positive electrode film, IKB, LIC7.2, and PTFE were firstly mixed in a mortar and pestle in a mass ratio of 50:50:1 to form the film. The initial film was manually rolled and cut out to 40 × 40 mm, then the film was continued to be thinned and enlarged by a roller press and cut to 40 × 40 mm, and

the rolling process was repeated about 3–4 times (the last time the electrode film was cut to 38 × 38 mm size). The pouch cells were then encapsulated in vacuum in an aluminum plastic film with a diameter of 60 mm. Galvanostatic charge/discharge tests of the ASS Li||I₂ battery were carried out by the Neware battery test system (CT-4008T, Shenzhen, China). The CV measurements were performed on the Bio-Logic VSP-300. Unless otherwise noted, all electrochemical tests were performed in a thermostatic test chamber maintained at a temperature of ~25 °C.

DFT calculations

All computations used VASP package with PAW pseudo-potentials. Exchange-correlation energetics of electrons were computed utilizing PBE functionals within the GGA framework. The simulations maintained a consistent plane wave basis cutoff energy of 520 eV throughout all calculations. For all calculations in this work, the cutoff energy of the plane wave was set to be 520 eV. The convergence criteria for energy and force are set to be less than 10⁻⁵ eV and 0.02 eV Å⁻¹. Spin polarization is turned on for all calculations. LIC7.2 and LYB have the same crystal structure (space group: C2/m), and the (001) surface was considered to be the main exposed surface for catalysis in this work. The slab model was constructed using 2 × 2 supercells and a vacuum layer of 20 Å was applied in the z-direction of the slab models to avoid the effect of periodic boundaries. For the k-points sampling of Brillouin-zone integrals, the Monkhorst-Pack grids were set to be 2 × 2 × 1. The cohesive energies were defined as

$$\Delta E = \frac{E_{\text{sys}} - E_{\text{sub}} - nE_{\text{atom}}}{n}$$

where E_{sys} , E_{sub} and E_{atom} represent the energies of the system, LIC7.2 or LYB substrate and isolated atoms such as Li, I, Cl, Br; and n means the number of isolated atoms. The selection criterion of the two-dimensional charge density sections is to display the charge information of I–Cl and I–Br as much as possible. Thus, all the two-dimensional charge density sections were cut from the center of I and its most adjacent Cl or Br atoms. All charge density maps were drawn with the same parameters. The isosurface level was set to 0.08 e/bohr³. For more accurate charge information of I–Cl and I–Br, the Bader charge was calculated. The employed DFT structures can be seen in Supplementary Data 1–6.

Data availability

The datasets generated and analyzed in this work are included in this article and Supplementary Information. Source data are provided with this paper.

References

- Manthiram, A. A reflection on lithium-ion battery cathode chemistry. *Nat. Commun.* **11**, 1550 (2020).
- Lee, W. et al. Advances in the cathode materials for lithium rechargeable batteries. *Angew. Chem. Int. Ed.* **59**, 2578–2605 (2020).
- He, W. et al. Challenges and recent advances in high capacity Li-rich cathode materials for high energy density lithium-ion batteries. *Adv. Mater.* **33**, 2005937 (2021).
- Jiao, S., Wang, J., Hu, Y.-S., Yu, X. & Li, H. High-capacity oxide cathode beyond 300 mAh/g. *ACS Energy Lett.* **8**, 3025–3037 (2023).
- Zhang, R. et al. Compositionally complex doping for zero-strain zero-cobalt layered cathodes. *Nature* 1–7, <https://doi.org/10.1038/s41586-022-05115-z> (2022).
- Li, K. et al. A 3D and stable lithium anode for high-performance lithium–iodine batteries. *Adv. Mater.* **31**, 1902399 (2019).

- Xu, J., Ma, J., Fan, Q., Guo, S. & Dou, S. Recent progress in the design of advanced cathode materials and battery models for high-performance lithium-X (X = O₂, S, Se, Te, I₂, Br₂) batteries. *Adv. Mater.* **29**, 1606454 (2017).
- Ma, J., Liu, M., He, Y. & Zhang, J. Iodine redox chemistry in rechargeable batteries. *Angew. Chem. Int. Ed.* **60**, 12636–12647 (2021).
- Chen, Q., Chen, S., Ma, J., Ding, S. & Zhang, J. Separation effect of graphene sheets with N, O codoping and molybdenum clusters for reversible lithium–iodine batteries. *Adv. Funct. Mater.* **34**, 2308272 (2024).
- Zhou, L. et al. High areal capacity, long cycle life 4 V ceramic all-solid-state Li-ion batteries enabled by chloride solid electrolytes. *Nat. Energy* <https://doi.org/10.1038/s41560-021-00952-0> (2022).
- Pan, H. et al. Carbon-free and binder-free Li–Al alloy anode enabling an all-solid-state Li–S battery with high energy and stability. *Sci. Adv.* **8**, eabn4372 (2022).
- Cheng, Z. et al. Achieving long cycle life for all-solid-state rechargeable Li–I₂ battery by a confined dissolution strategy. *Nat. Commun.* **13**, 125 (2022).
- Ma, W. et al. A twelve-electron conversion iodine cathode enabled by interhalogen chemistry in aqueous solution. *Nat. Commun.* **14**, 5508 (2023).
- Xie, C. et al. Reversible multielectron transfer I[−]/IO₃[−] cathode enabled by a hetero-halogen electrolyte for high-energy-density aqueous batteries. *Nat. Energy* 1–11, <https://doi.org/10.1038/s41560-024-01515-9> (2024).
- Li, X. et al. Activating the IO₃[−]/I[−] redox couple in an aqueous I₂–Zn battery to achieve a high voltage plateau. *Energy Environ. Sci.* **14**, 407–413 (2021).
- Zou, Y. et al. A four-electron Zn–I₂ aqueous battery enabled by reversible I[−]/I₂/I[−] conversion. *Nat. Commun.* **12**, 170 (2021).
- Chen, S. et al. Unraveling electrochemical stability and reversible redox of Y-doped Li₂ZrCl₆ solid electrolytes. *Energy Mater. Adv.* **4**, 0019 (2023).
- Jung, N., Crowther, A. C., Kim, N., Kim, P. & Brus, L. Raman enhancement on graphene: adsorbed and intercalated molecular species. *ACS Nano* **4**, 7005–7013 (2010).
- Hu, R. et al. Dramatically enhanced reversibility of Li₂O in SnO₂-based electrodes: the effect of nanostructure on high initial reversible capacity. *Energy Environ. Sci.* **9**, 595–603 (2016).
- Sun, Y. et al. High-capacity battery cathode prelithiation to offset initial lithium loss. *Nat. Energy* **1**, 15008 (2016).
- Dong, W. et al. A robust and conductive black tin oxide nanostructure makes efficient lithium-ion batteries possible. *Adv. Mater.* **29**, 1700136 (2017).
- Zhao, Q., Lu, Y., Zhu, Z., Tao, Z. & Chen, J. Rechargeable lithium–iodine batteries with iodine/nanoporous carbon cathode. *Nano Lett.* **15**, 5982–5987 (2015).
- Lu, P. et al. Wide-temperature, long-cycling, and high-loading pyrite all-solid-state batteries enabled by argyrodite thioarsenate superionic conductor. *Adv. Funct. Mater.* **33**, 2211211 (2023).
- Kim, K. et al. Material design strategy for halide solid electrolytes Li₃MX₆ (X = Cl, Br, and I) for all-solid-state high-voltage Li-ion batteries. *Chem. Mater.* **33**, 3669–3677 (2021).
- Park, D. et al. Theoretical design of lithium chloride superionic conductors for all-solid-state high-voltage lithium-ion batteries. *ACS Appl. Mater. Interfaces* **12**, 34806–34814 (2020).
- Wang, X. et al. Influence mechanism of interfacial oxidation of Li₃YCl₆ solid electrolyte on reduction potential. *Chem. Eur. J.* **30**, e202303884 (2024).
- Schwietert, T. K. et al. Clarifying the relationship between redox activity and electrochemical stability in solid electrolytes. *Nat. Mater.* **19**, 428–435 (2020).
- Schwietert, T. K., Vasileiadis, A. & Wagemaker, M. First-principles prediction of the electrochemical stability and reaction mechanisms of solid-state electrolytes. *JACS Au* **1**, 1488–1496 (2021).
- Li, C. et al. Highly reversible Zn metal anode securing by functional electrolyte modulation. *Adv. Energy Mater.* **14**, 2400872 (2024).
- Zhang, P.-F. et al. Toward shuttle-free Zn–I₂ battery: anchoring and catalyzing iodine conversion by high-density P-doping sites in carbon host. *Adv. Funct. Mater.* **34**, 2306359 (2024).
- Wang, T. et al. Surface patterning of metal zinc electrode with an In-region zincophilic interface for high-rate and long-cycle-life zinc metal anode. *Nano-Micro Lett* **16**, 112 (2024).
- Koerver, R. et al. Chemo-mechanical expansion of lithium electrode materials—on the route to mechanically optimized all-solid-state batteries. *Energy Environ. Sci.* **11**, 2142–2158 (2018).
- Tan, D. H. S., Banerjee, A., Chen, Z. & Meng, Y. S. From nanoscale interface characterization to sustainable energy storage using all-solid-state batteries. *Nat. Nanotechnol.* **15**, 170–180 (2020).
- Liu, Y., He, P. & Zhou, H. Rechargeable solid-state Li–Air and Li–S batteries: materials, construction, and challenges. *Adv. Energy Mater.* **8**, 1701602 (2018).
- Sun, X. et al. Tailoring electronic-ionic local environment for solid-state Li–O₂ battery by engineering crystal structure. *Sci. Adv.* **8**, eabq6261 (2022).
- Kondori, A. et al. A room temperature rechargeable Li₂O-based lithium–air battery enabled by a solid electrolyte. *Science* **379**, 499–505 (2023).
- Wang, D. et al. Realizing high-capacity all-solid-state lithium–sulfur batteries using a low-density inorganic solid-state electrolyte. *Nat. Commun.* **14**, 1895 (2023).
- Alzahrani, A. S. et al. Confining sulfur in porous carbon by vapor deposition to achieve high-performance cathode for all-solid-state lithium–sulfur batteries. *ACS Energy Lett.* **6**, 413–418 (2021).
- Kim, J. T. et al. Manipulating Li₂S₂/Li₂S mixed discharge products of all-solid-state lithium sulfur batteries for improved cycle life. *Nat. Commun.* **14**, 6404 (2023).
- Li, X. et al. Water-mediated synthesis of a superionic halide solid electrolyte. *Angew. Chem. Int. Ed.* **58**, 16427–16432 (2019).
- Li, H., Lyu, Z. & Han, M. Robust and fast estimation of equivalent circuit model from noisy electrochemical impedance spectra. *Electrochim. Acta* **422**, 140474 (2022).

Acknowledgements

This research was supported by the National Key R&D Program of China (2021YFB3800300—P.H. and H.Z.), the National Natural Science Foundation of China (923722201—H.Z., 22179059—P.H., 22239002—H.Z.), Key R&D project funded by department of science and technology of Jiangsu Province (BE2020003—P.H.), science and technology innovation fund for emission peak and carbon neutrality of Jiangsu province (BK20231512—P.H., BK20220034—H.Z.).

Author contributions

P.H. and H.Z. conceived the idea and supervised the research. Z.C. and H.L. conducted the experiments. M.Z. performed the DFT calculations. Z.C., H.L., and P. H. analyzed the experiment results and wrote the manuscript. H.P., C.S., W.L., and M.W. discussed the results and commented on the manuscript. Z.C. and H.L. contributed equally to this work.

Competing interests

The authors declare no competing interests.

Additional information

Supplementary information The online version contains supplementary material available at <https://doi.org/10.1038/s41467-025-56932-5>.

Correspondence and requests for materials should be addressed to Ping He or Haoshen Zhou.

Peer review information *Nature Communications* thanks Diyi Cheng, Guanzhou Zhu, and the other, anonymous, reviewer(s) for their contribution to the peer review of this work. A peer review file is available.

Reprints and permissions information is available at <http://www.nature.com/reprints>

Publisher's note Springer Nature remains neutral with regard to jurisdictional claims in published maps and institutional affiliations.

Open Access This article is licensed under a Creative Commons Attribution 4.0 International License, which permits use, sharing, adaptation, distribution and reproduction in any medium or format, as long as you give appropriate credit to the original author(s) and the source, provide a link to the Creative Commons licence, and indicate if changes were made. The images or other third party material in this article are included in the article's Creative Commons licence, unless indicated otherwise in a credit line to the material. If material is not included in the article's Creative Commons licence and your intended use is not permitted by statutory regulation or exceeds the permitted use, you will need to obtain permission directly from the copyright holder. To view a copy of this licence, visit <http://creativecommons.org/licenses/by/4.0/>.

© The Author(s) 2025